



Cite this: *Nanoscale*, 2022, **14**, 10929

# Molecular simulations of the interfacial properties in silk–hydroxyapatite composites†

Diego López Barreiro, <sup>‡a</sup> Zaira Martín-Moldes, <sup>‡a,b</sup>  
 Adrián Blanco Fernández, <sup>c</sup> Vincent Fitzpatrick, <sup>b</sup> David L. Kaplan <sup>b</sup> and  
 Markus J. Buehler <sup>\*a,d</sup>

Biom mineralization is a common strategy used in Nature to improve the mechanical strength and toughness of biological materials. This strategy, applied in materials like bone or nacre, serves as inspiration for materials scientists and engineers to design new materials for applications in healthcare, soft robotics or the environment. In this regard, composites consisting of silk and hydroxyapatite have been extensively researched for bone regeneration applications, due to their reported cytocompatibility and osteoinduction capacity that supports bone formation *in vivo*. Thus, it becomes relevant to understand how silk and hydroxyapatite interact at their interface, and how this affects the overall mechanical properties of these composites. This theoretical–experimental work investigates the interfacial dynamic and structural properties of silk in contact with hydroxyapatite, combining molecular dynamics simulations with analytical characterization. Our data indicate that hydroxyapatite decreases the  $\beta$ -sheets in silk, which are a key load-bearing element of silk. The  $\beta$ -sheets content can usually be increased in silk biomaterials *via* post-processing methods, such as water vapor annealing. However, the presence of hydroxyapatite appears to reduce also for the formation of  $\beta$ -sheets *via* water vapor annealing. This work sheds light into the interfacial properties of silk–hydroxyapatite composite and their relevance for the design of composite biomaterials for bone regeneration.

Received 11th April 2022,  
 Accepted 10th July 2022  
 DOI: 10.1039/d2nr01989b  
[rsc.li/nanoscale](http://rsc.li/nanoscale)

## 1. Introduction

Bone is a biomineralized composite whose main components are collagen and carbonate-substituted hydroxyapatite minerals.<sup>1,2</sup> Although bone has an innate capacity to self-regenerate, there is great interest in the tissue engineering field for developing robust and lightweight biomaterials that stimulate, control and accelerate the repair of large bone defects. Such biomaterials are usually three-dimensional

scaffolds that combine polymers and inorganic osteoinductive materials. Synthetic polymers, such as polycaprolactone (PCL), polyglycolic acid (PGA), polylactic acid (PLA) or poly(lactic-co-glycolic acid) (PLGA) are commonly used.<sup>3,4</sup> However, there is an increased shift towards the use of natural biopolymers, including silk, collagen, alginate or chitosan, due their biocompatibility and biodegradability, as well as their versatile aqueous processing into useful biomaterial formats.<sup>4–7</sup> Moreover, recombinant DNA technology and developments in bioprocess engineering increasingly enable the use of fermentative processes for the biofabrication of rationally-designed protein biopolymers. This allows to rationally design novel protein biopolymers with fit-for-purpose physicochemical and biological properties<sup>8</sup> while reducing our dependence on animal sources for their production.

Silk proteins from *Bombyx mori* cocoons have outstanding mechanical properties that arise from a hierarchical structure.<sup>9,10</sup> Silk is characterized by a high extensibility and toughness,<sup>11</sup> and has been successfully applied as a soft matrix for the manufacturing of materials and composites with applications in biomedicine,<sup>12</sup> flexible electronics<sup>13</sup> and water purification,<sup>14</sup> among many other areas of utility. The crystalline domain in silk (with repetitive motifs including GAGAGA, GAGAGS, GAGAGY, or GAGYGA) is composed of

<sup>a</sup>Laboratory for Atomistic and Molecular Mechanics (LAMM), 77 Massachusetts Avenue, 1-165, Cambridge, MA 02139, USA. E-mail: [mbuehler@MIT.EDU](mailto:mbuehler@MIT.EDU);

Fax: +1.617.452.2750; Tel: +1.617.452.2750

<sup>b</sup>Department of Biomedical Engineering, Tufts University, 4 Colby Street, Medford, MA 02155, USA

<sup>c</sup>Instituto de Cerámica de Galicia (ICG), Universidade de Santiago de Compostela, Avda. do Mestre Mateo, 25, 15706 Santiago de Compostela, A Coruña, Spain

<sup>d</sup>Center for Computational Science and Engineering, Schwarzman College of Computing, Massachusetts Institute of Technology, 77 Massachusetts Ave., Cambridge, MA 02139, USA

†Electronic supplementary information (ESI) available: Preparation of hydroxyapatite surfaces resolved at pH 7, FTIR spectra of HAP and silk–HAP, deconvolution of the amide I peak for different silk–HAP materials. See DOI: <https://doi.org/10.1039/d2nr01989b>

\*These authors contributed equally to this work.



stacks of hydrophobic anti-parallel  $\beta$ -sheets held together by hydrogen bonds.<sup>15,16</sup> The amorphous domain (with the amino acid sequence TGSSGFGPYVANGGYSGYEWSSSEDFGTGS)<sup>17,18</sup> constitutes the hydrophilic matrix in which the  $\beta$ -sheet crystals are embedded. The crystalline domains provide mechanical strength, whereas the amorphous domains provide flexibility and toughness.<sup>19</sup> Last, the N-terminus has been suggested to play a key role in the self-assembly of silk into fibers.<sup>20</sup>

Although silk can be used for the fabrication of biomaterials that mimic the extracellular matrix, inherent osteoinductivity is absent.<sup>21</sup> Thus, osteoinductive components need to be embedded in the silk matrix to enhance bone tissue regeneration. Several candidates are being investigated, including apatites,<sup>22,23</sup> silica<sup>24,25</sup> or bioactive glass.<sup>26,27</sup> Particularly, hydroxyapatite (HAP) is an appealing choice<sup>4</sup> because HAP has a chemical structure similar to that of the mineral components of natural bone, and silk can template the growth of HAP crystals along its fibers.<sup>28,29</sup> Materials containing different forms of HAP (e.g., powder, nanoparticles) have shown osteogenic differentiation capacity *in vitro*, while supporting bone formation *in vivo* when blended with silk into composites.<sup>21,30–33</sup> Moreover, the addition of silk has shown to improve the compressive strength and Young's modulus of HAP-based materials.<sup>34</sup>

Several approaches can be followed to prepare silk–HAP composites: mixing HAP and silk in solution,<sup>30,34</sup> mineralizing preformed silk scaffolds in solutions containing precursor salts of HAP,<sup>35,36</sup> or using recombinant chimeric silk-like polypeptides fused to biomineralization domains that nucleate the growth of HAP crystals.<sup>37</sup> Regardless of the approach followed, the morphological, mechanical and structural properties of silk–HAP composites will impact their *in vivo* behavior and bone regeneration potential.<sup>23</sup> These properties can be severely affected by the interfacial interactions between silk and HAP.<sup>38</sup> Most of the research so far has focused on the biomineralization of the whole silk protein, with only a limited number of studies dissecting the interactions of each silk domain with HAP.<sup>28</sup> This study addresses that gap by applying molecular dynamics (MD) simulations to unveil how the different domains in silk (amorphous, crystalline and N-terminus) interact with HAP. MD simulations can uncover structural and dynamic features of biomolecules with atomistic resolution. They have been successfully applied to study the interfacial properties of silk in contact with substrates like graphene<sup>39</sup> and silica.<sup>40</sup> MD literature pertaining silk–HAP composites mainly encompasses coarse grain simulations for applications like water filtration,<sup>29</sup> or bioinspired self-folding materials.<sup>41</sup> Here, we used fully atomistic MD simulations instead to investigate how the amorphous, crystalline and N-terminus silk domains interact with HAP (001) surfaces. These simulations revealed with atomistic resolution important interfacial features in silk–HAP composites, such as hydrogen bonding patterns, changes in secondary structure, or key interacting amino acids. The simulation results were complemented with experimental data obtained *via* FTIR. This allowed us to gain further insight into how the secondary structure of silk is

impacted by the presence of HAP and the use a common consolidation method for silk biomaterials, water vapor annealing. Overall, our computational–experimental data suggest that HAP reduced the content of ordered, load-bearing  $\beta$ -sheet crystals in silk. This decrease was only partially overcome by the use of water vapor annealing. These results deepen our understanding of the interfacial phenomena occurring in silk–HAP composites while providing guidelines for controlling their mechanical properties.

## 2. Materials and methods

### 2.1. Computational modeling and simulations

The HAP (001) surface was used for these simulations.<sup>42–44</sup> This surface is commonly used in computational simulations pertaining the interaction of HAP with biomacromolecules.<sup>45–47</sup> The protonation of the inorganic–aqueous interface due to the presence of water is critical for MD simulations involving HAP and proteins, but this issue is oftentimes overlooked in computational studies. To that end, the Interface Force Field provides pH-resolved surface models of the HAP (001) surface at pH 5.<sup>44,48</sup> Those surface models were used here to generate models at pH 7 by adjusting the protonation state, atomic environment and atomic charges on the hydroxyapatite surface (Fig. S1†). The software Materials Studio 4.4<sup>49</sup> was used to protonate several  $\text{H}_2\text{PO}_4^-$  surface groups, until the concentration of surface  $\text{H}_2\text{PO}_4^-$  and  $\text{HPO}_4^{2-}$  groups became equal. Accordingly, the partial charges were modified for those surface-exposed dihydrogen phosphate groups deprotonated to monohydrogen phosphate. By increasing the pH from 5 to 7, one calcium ion was added for every two new monohydrogen phosphate groups to maintain charge neutrality.

We used MD simulations to investigate the dynamic properties of the amorphous domain,  $\beta$ -sheet crystals and N-terminus of silk in contact with HAP at pH 7 (Fig. 1). Silk's crystalline structure and the N-terminus were obtained from the Protein Data Bank (PDB) files with the codes 2SLK and 3UA0, respectively. 2SLK is formed by a 3-layer stack of antiparallel  $\beta$  sheets. Each layer contains five antiparallel peptide chains with the sequence GAGAGS. 3UA0 is a homodimer forming an eight-stranded  $\beta$ -sheet.<sup>50</sup> 12 peptide chains with the sequence TGSSGFGPYVANGGYSGYEWSSSEDFGTGS<sup>17,18</sup> in a 3 by 4 arrangement were used to create the amorphous domain, following the procedure outlined elsewhere.<sup>13</sup>

MD simulations were performed in NAMD 2.13,<sup>51</sup> using the Chemistry at HARvard Macromolecular Mechanics (CHARMM)<sup>52</sup> force field for the solvated protein system and the Interface Force Field<sup>48</sup> for HAP. The simulated systems intended to represent typical conditions used in the *ex vivo* preparation of silk–HAP scaffolds e.g., *via* 3D printing.<sup>34</sup> The starting structures for the crystalline, amorphous and N-terminus domains were placed 5 Å above the HAP surface. The systems were solvated in a TIP3P water box with periodic boundary conditions and  $\text{Na}^+$  and  $\text{Cl}^-$  ions were added as needed to neutralize the total charge of the system. The system



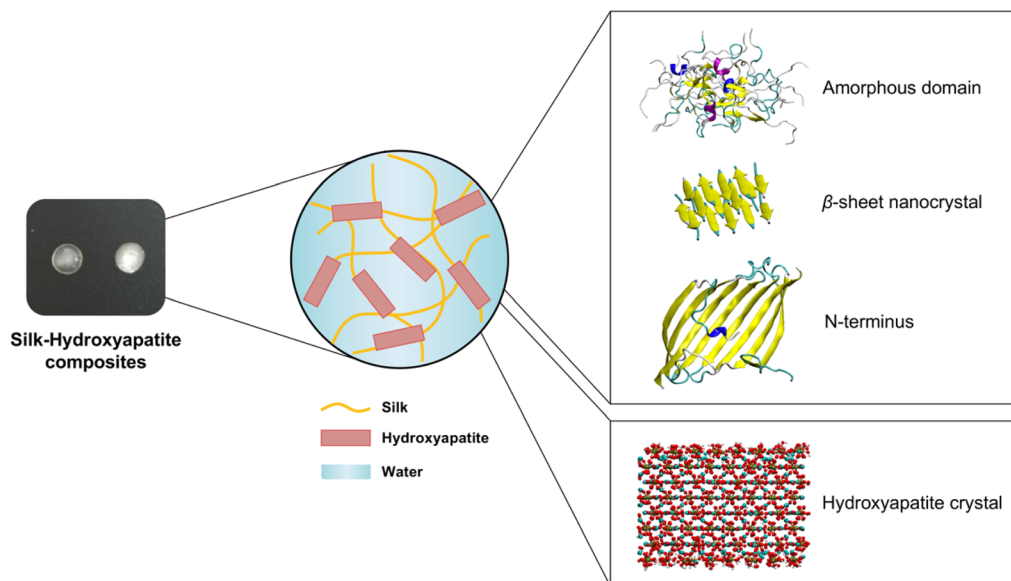


**Fig. 1** The objective of this work is to investigate the interfacial dynamic and structural properties of three different silk domains (amorphous, crystalline and N-terminus) in contact with HAP surfaces, and their implications for the bottom-up design of mineralized materials with controlled structural and mechanical properties. In this figure, a schematic representation of silk–HAP composites is shown, including snapshots of the initial configuration of the silk domains and the HAP unit cell used for MD simulations.

dimensions were only allowed to change in the  $z$  direction, keeping the  $x$ – $y$  plane dimensions fixed. The ShakeH algorithm<sup>53</sup> was applied to all the bonds including hydrogen atoms. In all cases, 3D periodic boundary conditions were applied. The solvation box was made sufficiently large in the vertical direction to avoid spurious effects of self-interactions for the HAP–protein system.

The energy of the systems was minimized, followed by Langevin dynamics for 125 ns using the NPT ensemble at 300 K. Pressure (1 bar) was exerted through the Nosé–Hoover Langevin piston. The long-range electrostatic coulombic interactions were calculated using the particle mesh Ewald (PME) method with a grid spacing of 1 Å with periodic boundary conditions. A cutoff distance of 12 Å was applied for electrostatic and van der Waals interactions of the explicit solvent replicas, with a switch distance of 10 Å to avoid hard cuts. The timestep chosen was 2 fs. The position of the backbone of the peptide structures was restrained for the first 1 ns of simulation. The bulk of the hydroxyapatite atoms was kept fixed throughout the entire simulation, only allowing to move the most external atoms on the top and bottom surfaces. Three replicas were performed for each system, and simulation data was output every 0.2 ns.

## 2.2. Data analysis of MD simulations

Data produced during the simulations were analyzed using in-house TCL and Python scripts. Atomic structures were visualized using the Visual Molecular Dynamics (VMD) graphics software.<sup>54</sup> The evolution of the root mean square deviation (RMSD) of the atomic positions during the simulation was analyzed for the protein backbone using the RMSD Trajectory

Tool from VMD. The count of intraprotein and protein–HAP hydrogen bonds throughout the simulation trajectories was analyzed using the Hbonds plugin from VMD, following its default geometric criteria (distance cutoff of 3.0 Å and a D–H–A angle cutoff of 20°). Custom TCL scripts were developed to analyze in VMD the solvent accessible surface area (SASA) (using a standard water probe radius of 1.4 Å), the radius of gyration of the protein domains, and the evolution of the protein's secondary structure with the STRIDE algorithm.<sup>55</sup> Close contacts between the protein domains and HAP were defined as contacts with a distance below 4 Å, excluding hydrogen atoms.

## 2.3. Preparation of silk–HAP films

The silk solution used for film preparation was prepared as described previously.<sup>56</sup> Briefly, pieces of *Bombyx mori* cocoons (5 g) were boiled for 30 minutes in 0.02 M aqueous  $\text{Na}_2\text{CO}_3$ , rinsed extensively in  $\text{dH}_2\text{O}$  and dried overnight. Dry silk was then dissolved in 9.3 M aqueous LiBr solution at 60 °C for 4 hours. The silk/LiBr solution was dialyzed against distilled water for 2 days, with 10 water changes. The resulting solution was centrifuged at 9000 rpm at 4 °C twice for 20 min. The concentration of the silk solution was determined by calculating the weight ratio between the wet and dry solution. The extracted silk in solution was diluted to a concentration of 5% (w/v) in water. Commercial HAP (MP Biomedicals, Solon, OH, US, purity >99.99%) was dispersed in water by sonication and then mixed with the silk solution to obtain a suspension with HAP : silk ratios of 1, 5 or 10 wt%.

For characterization purposes, multiple films of each sample were prepared by depositing 30  $\mu\text{L}$  of each dissolved



protein solutions onto different polydimethylsiloxane (PDMS) disks ( $R = 6$  mm). Water vapor annealing experiments to induce  $\beta$ -sheet formation in silk films were performed using an isotemp vacuum oven for 24 h at room temperature, and then air dried.<sup>57</sup> Scanning Electron Microscopy (SEM) of silk and silk-HAP films was performed on a Zeiss EVO-10MA microscope (Zeiss, Oberkochen, Germany) at 5 kV accelerating voltage. Prior to imaging, the samples were rapidly frozen with liquid nitrogen, cryofractured to expose the cross-sections, and coated with  $\sim 10$  nm gold using a SC7620 sputter coater (Quorum Technologies, UK).

#### 2.4. Analysis of the secondary structure of silk-HAP films

Fourier Transform Infrared Spectroscopy (FTIR) of the films was carried out with an Attenuated Total Reflectance FTIR machine (Jasco, Oklahoma City, OK, USA). Films were measured using five independent replicas. 64 scans with a resolution of  $4\text{ cm}^{-1}$  were recorded and averaged in the range of 400 to  $4000\text{ cm}^{-1}$  for each sample. The protein secondary structure composition was determined by performing peak deconvolution over the amide I region ( $1595\text{--}1705\text{ cm}^{-1}$ ) with an in-house Python script using the lmfit package for curve fitting. This region is the most sensitive spectral region to protein secondary structure, which originates from the  $\text{C}=\text{O}$

stretching vibration of the amide group coupled with the in-phase bending of the N-H bond and stretching of the C-N bond.<sup>58,59</sup> The baseline was corrected by fitting a straight line between the  $1595\text{--}1705\text{ cm}^{-1}$  region. The deconvolution was carried out using five primary peaks assigned to different secondary structures:  $1620\text{ cm}^{-1}$  ( $\beta$ -sheet),  $1645$ ,  $1660$  and  $1670\text{ cm}^{-1}$  (random coil/helix), and  $1700\text{ cm}^{-1}$  (turn).<sup>60</sup> The peak positions were allowed to shift  $4\text{ cm}^{-1}$  using the Levenberg-Marquardt algorithm, and a Gaussian model was selected for the band shape. A nonlinear least-squares method was used to obtain a reconstituted curve as close as possible to the original spectra. The statistical significance of the numerical values reported was assessed *via* a one-way analysis of variance (ANOVA) test.

### 3. Results

#### 3.1. Molecular dynamics simulations

The simulation results indicated that the three silk domains adsorbed on HAP (001) surfaces at pH 7 (Fig. 2), but the structural consequences of this adsorption were different for each domain. The following section reports these consequences in terms of hydrogen bonding, silk-HAP close contacting amino acids, radius of gyration, root mean square deviation (RMSD)

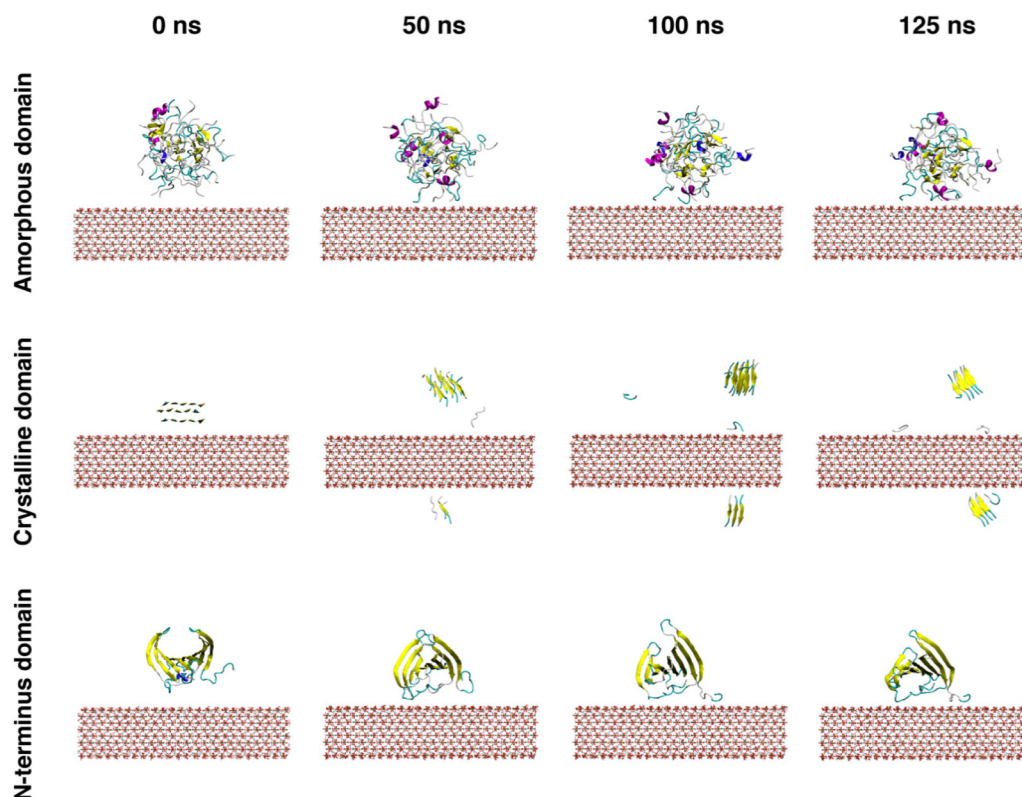


**Fig. 2** Depiction of MD snapshots of the interaction between the amorphous, crystalline and N-terminus domains of silk and HAP (001) surfaces resolved for pH 7. HAP atoms are plotted using the CPK representation, whereas the various silk domains are plotted using the cartoon representation. Water molecules and  $\text{Na}^+$  and  $\text{Cl}^-$  ions are not shown for clarity. With regard to the secondary structures in silk domains,  $\alpha$ -helices are colored in purple,  $3_{10}$  helices in blue,  $\beta$ -strands in yellow, turns in cyan and random coil regions white.





of atomic positions, solvent accessible surface area (SASA) and secondary structure. The evolution of those parameters during the simulation is plotted in Fig. 3, and average values for the first and the last 5 ns of simulation are reported in Table 1.

**3.1.1. Amorphous domain.** Close contacts between the amorphous domain of silk and the HAP (001) surface took place predominantly through the negatively charged side

chain of glutamic acids. HAP formed hydrogen bonds with the amorphous domain (Fig. 3a) and induced an increase in intraprotein hydrogen bonds from  $35 \pm 3$  to  $45 \pm 2$  (Fig. 3b). This increase did not cause any major change in the shape of the domain, as shown by the negligible variation of its radius of gyration (from  $21.8 \pm 0.1$  to  $21.7 \pm 0.1$  Å) (Fig. 3c). This was also confirmed visually during the simulation trajectory, as

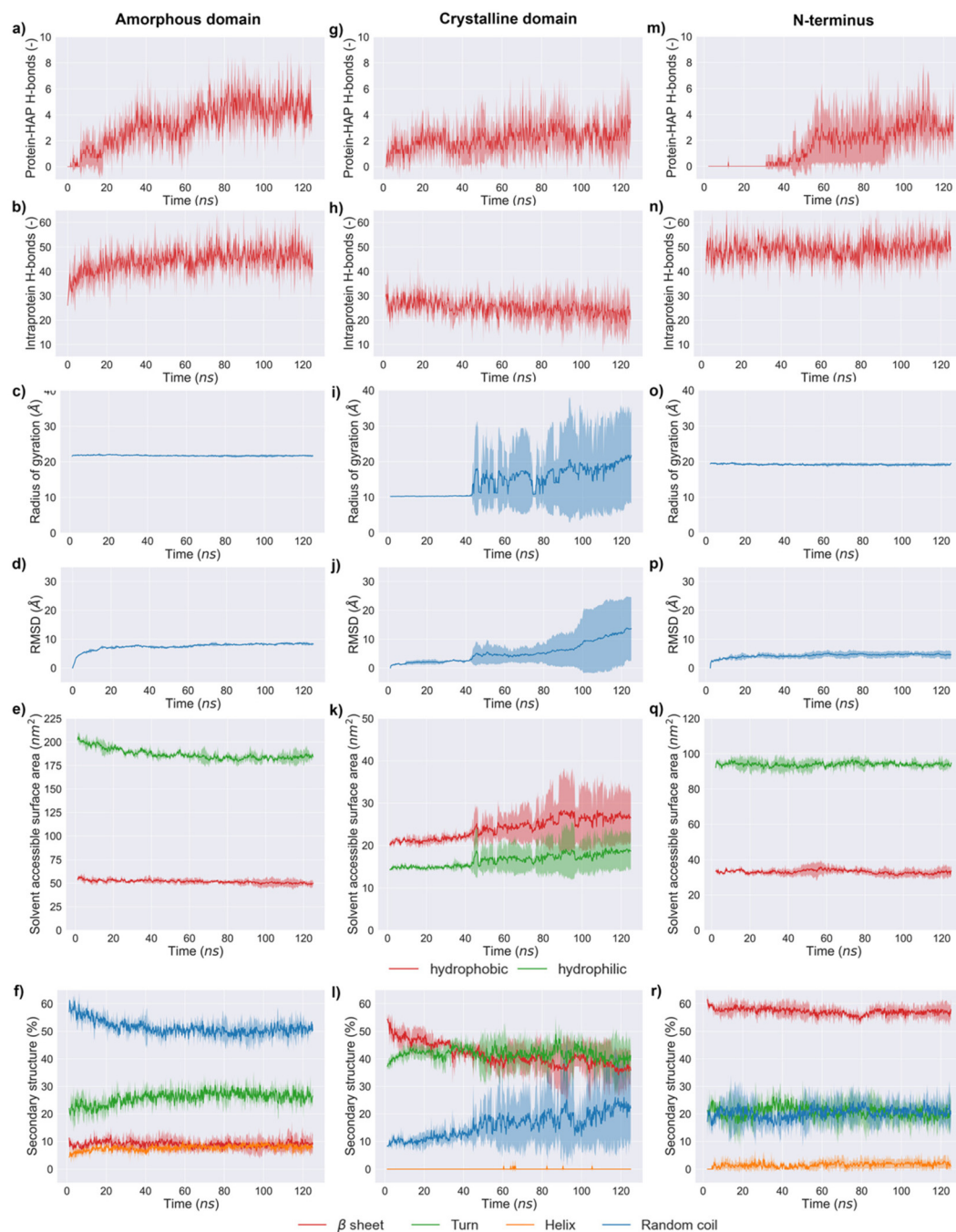


**Fig. 3** Temporal profile of key parameters during 125 ns of MD simulations: (a, g and m) protein–HAP hydrogen bonds for the different silk domains; (b, h and n) intraprotein hydrogen bonds for the different silk domains; (c, i and o) radius of gyration of silk domains; (d, j and p) root mean square displacement (RMSD) of silk domains; (e, k and q) solvent accessible surface area (SASA) of hydrophobic and hydrophilic amino acids in silk; (f, l and r) secondary structure of silk domains.



**Table 1** Average values ( $\pm$  standard deviation) during the initial and final 5 ns of simulation of various parameters calculated for silk–HAP MD simulations (replicates = 3)

		Secondary structure (%)						
		Protein-HAP H-bonds	Intraprotein H-bonds	SASA <sub>hydrophobic</sub> (nm <sup>2</sup> )	SASA <sub>hydrophilic</sub> (nm <sup>2</sup> )	R <sub>grr</sub> (Å)	RMSD (Å)	
<b>Amorphous domain</b>								
	Initial 5 ns	0 $\pm$ 0	35 $\pm$ 3	55.0 $\pm$ 1.5	201.1 $\pm$ 2.7	21.8 $\pm$ 0.1	3.9 $\pm$ 1.2	8.7 $\pm$ 1.1
	Final 5 ns	4 $\pm$ 1	45 $\pm$ 2	49.6 $\pm$ 0.8	185.2 $\pm$ 1.4	21.7 $\pm$ 0.1	8.4 $\pm$ 1.2	9.1 $\pm$ 0.6
								Turn
								Random coil
								Helix
								5.3 $\pm$ 0.8
								8.0 $\pm$ 0.6
<b>Crystalline domain</b>								
	Initial 5 ns	1 $\pm$ 0	27 $\pm$ 3	20.8 $\pm$ 0.5	14.7 $\pm$ 0.3	10.2 $\pm$ 0.0	1.1 $\pm$ 0.3	51.1 $\pm$ 2.3
	Final 5 ns	3 $\pm$ 1	23 $\pm$ 2	26.7 $\pm$ 0.3	18.7 $\pm$ 0.2	21.0 $\pm$ 0.5	13.1 $\pm$ 0.7	36.4 $\pm$ 0.8
								Turn
								Random coil
								Helix
								0.0 $\pm$ 0.0
								0.0 $\pm$ 0.0
<b>N-terminus domain</b>								
	Initial 5 ns	0 $\pm$ 0	48 $\pm$ 4	33.1 $\pm$ 0.6	94.3 $\pm$ 0.9	19.5 $\pm$ 0.1	2.2 $\pm$ 0.7	59.6 $\pm$ 0.7
	Final 5 ns	3 $\pm$ 1	51 $\pm$ 3	33.1 $\pm$ 0.6	93.8 $\pm$ 0.7	19.2 $\pm$ 0.1	4.6 $\pm$ 0.1	57.1 $\pm$ 0.6
								Turn
								Random coil
								Helix
								0.1 $\pm$ 0.3
								2.0 $\pm$ 0.7

shown in the snapshots in Fig. 2. In fact, the amorphous domain quickly attained a stable conformation on the first 5–10 ns of simulation, as shown by the stability of its RMSD (Fig. 3d). The solvent accessible surface area (SASA) of the amorphous domain remained stable during the simulation, showing only a small reduction in its value for the hydrophilic residues (Fig. 3e). Overall, its secondary structure remained highly disordered (Fig. 3f). The random coil regions decreased from 58.0  $\pm$  1.6% in the starting structure to 51.0  $\pm$  1.0% during the last 5 ns of simulation, but this was countered by an increase in turn structures (21.7  $\pm$  1.5% at the beginning of the simulation, 26.2  $\pm$  1.4% at the end of the simulation).

**3.1.2. Crystalline domain.** The formation of hydrogen bonds between the crystalline domain and the HAP (001) surface showed an increased frequency as the simulation progressed (Fig. 3i), while the intraprotein hydrogen bonds steadily decreased from 27  $\pm$  3 to 23  $\pm$  2 (Fig. 3h). The crystalline domain underwent a severe structural reshuffling when interacting with the HAP (001) surface, as reflected by the large variation in its radius of gyration (from 10.2  $\pm$  0.0 to 21.0  $\pm$  0.5 Å) (Fig. 3i) and its RMSD (from 1.1  $\pm$  0.3 to 13.1  $\pm$  0.7 Å) (Fig. 3j). However, this disruption of the crystalline domain only took place after *ca.* 40 ns of simulation. Once the disruption was initiated, it was maintained for the remainder of the simulation. The SASA revealed that both the hydrophobic and hydrophilic amino acids became more exposed as the simulation progressed (Fig. 3k). This had a major effect on the secondary structure of this domain (Fig. 3l), causing a decrease of  $\beta$ -sheet structures (from 51.1  $\pm$  2.3 to 36.4  $\pm$  0.8%) and a concomitant rise in random coil structures (from 9.5  $\pm$  1.0 to 22.6  $\pm$  1.5%).

**3.1.3. N-terminus domain.** The close contacts between the N-terminus domain and the HAP (001) surface took place mostly through aspartic acid, tyrosine, lysine and asparagine residues in chain A; and aspartic acid, serine and glutamic acid residues in chain B. The interaction between the N-terminus and HAP (001) surface was not favored during the first part of the simulation. In fact, the N-terminus was only able to form hydrogen bonds with the HAP (001) surface after 50 ns of simulation (Fig. 3m). Intraprotein hydrogen bonds (Fig. 3n) and radius of gyration (Fig. 3o) remained stable throughout the simulation (from 48  $\pm$  4 to 51  $\pm$  3 and from 19.5  $\pm$  0.1 to 19.2  $\pm$  0.1 Å, respectively). The RMSD reached a stable value after the first 10 ns of simulation (Fig. 3p), and the SASA appeared also unaffected by the interaction with the HAP (001) surface (Fig. 3q). The secondary structure remained rather constant (Fig. 3r), with the content of  $\beta$ -sheets undergoing a minimal variation during 125 ns of simulation (from 59.6  $\pm$  0.7 to 57.1  $\pm$  0.6%).

### 3.2. Secondary structure of silk–HAP films

The secondary structure of silk films prepared with different HAP contents was analyzed by FTIR (Fig. 4a). The spectra showed the presence of a peak at 1040–960 cm<sup>−1</sup> in all samples with 10 wt% HAP, characteristic of the presence of PO<sub>4</sub><sup>3−</sup> ions from HAP.<sup>29,34,61</sup> Such a peak was not observed for the silk film control and silk films containing 1 wt% HAP



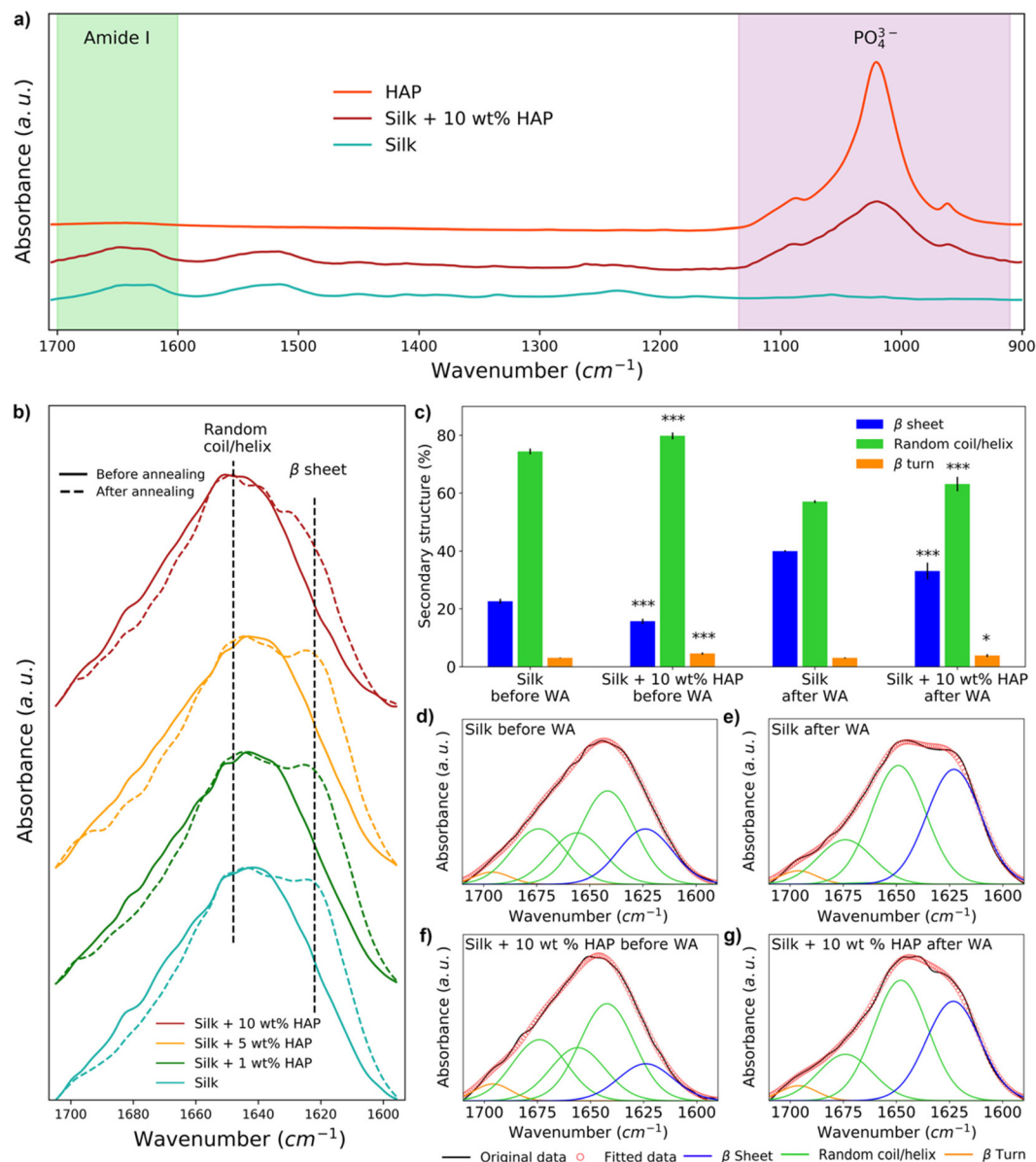


**Fig. 4** Analysis of the secondary structure of silk-HAP films with different HAP contents by means of Fourier-transform infrared spectroscopy (FTIR): (a) spectra of different silk-HAP films, highlighting peaks associated with the amide I region and the presence of phosphate groups from HAP; (b) amide I region for different silk-HAP regions, highlighting the position of peaks related to  $\beta$  sheets and random coil/helix secondary structures before and after water vapor annealing (WA); (c) quantitative analysis of the deconvolution of the amide I region (error bars represent standard deviation of the average of five individual samples); and (d-g) deconvoluted spectra of the amide I region of silk and silk-HAP 10 wt% films, highlighting the increase in  $\beta$  sheet structures after water vapor annealing (WA).

(Fig. S2†), and it was only present in some of the replicas with 5 wt% HAP (Fig. S3†), indicating an inhomogeneous distribution of the HAP particles at such low concentrations. HAP samples without silk did not show any relevant changes in their FTIR spectra before and after water vapor annealing (Fig. S4†), hinting that any changes observed after water vapor annealing in the amide I region were caused by changes in the silk component of the films.

The analysis of the spectra in the amide I region demonstrated that the water vapor annealing process caused an

increase in the absorption band at 1620 cm⁻¹ for all samples, which is associated with the presence of  $\beta$ -sheets (Fig. 4b). However, the intensity of the 1620 cm⁻¹ band decreased as the concentration of HAP increased (Fig. 4b). This was also noticeable by deconvoluting the spectra of silk and silk and silk-HAP 10 wt% films ( $p < 0.001$ ) (Fig. 4c-g). The deconvolution for films with 1 and 5 wt% HAP were not statistically different to the silk control films (Table S1†). Before water vapor annealing, silk films had a random coil/helix content of  $74.4 \pm 1.0\%$  and a  $\beta$ -sheet content of  $22.6 \pm 0.9\%$ , while for silk-HAP

10 wt% films the random coil/helix content was  $79.8 \pm 1.2\%$  and the  $\beta$ -sheet content  $15.7 \pm 0.9\%$ . After water vapor annealing the  $\beta$ -sheet content of the films increased to  $40.0 \pm 0.3\%$ , while the random coil/helix content decreased to  $57.0 \pm 0.5\%$ ; the increase in  $\beta$ -sheets after water vapor annealing was lower for silk-HAP 10 wt% films ( $33.1 \pm 2.9\%$ ), with a random coil/helix content of  $63.1 \pm 2.5\%$ . Although we report numerical values for the secondary structure obtained by this means, we note that this methodology is associated with some level of uncertainty as discussed elsewhere,<sup>62</sup> and therefore the deconvolution results should be interpreted as mere indicators of a trends, rather than as absolute values.

### 3.3. Surface characterization of silk-HAP films

SEM was used to assess the morphology of silk and silk-HAP films, as well as the distribution of HAP within the silk matrix. Given the differences identified for the secondary structure of silk and silk-HAP 10 wt% films, we analyzed their surface and cross-section. Silk control films were continuous and uniform (Fig. 5). In contrast, deposits of HAP crystals became visible on the surface of silk-HAP 10 wt% films, confirming a uniform distribution of HAP particles within the silk matrix.

## 4. Discussion

The ability of silk to induce HAP mineralization has been demonstrated under varied experimental conditions.<sup>21,30–33</sup> Here, we investigated the interfacial phenomena related to this process *via* fully atomistic MD simulations between three silk

domains and HAP (001) surfaces. Our results showed that silk was richer in disordered structures (random coil and turns) when in contact with the HAP (001) surface, which agreed with earlier experimental data.<sup>21</sup> The secondary structure of the crystalline domain of silk remained more stable than the amorphous and N-terminus domains during the first 40 ns of simulation. We attribute this to the stabilization effect of its highly concentrated network of hydrogen bonds, which required longer times to be disrupted by the HAP (001) surface. However, once the disruption was initiated, the crystal structure collapsed rapidly: random structures rose from  $9.5 \pm 1.0$  to  $22.6 \pm 1.5\%$  while  $\beta$ -sheets decreased from  $51.1 \pm 2.3$  to  $36.4 \pm 0.8\%$ . A similar effect was observed in MD simulations of silk  $\beta$ -sheet crystals in contact with silica surfaces.<sup>40</sup> This weakening of  $\beta$ -sheet crystals when in contact with HAP is relevant from a mechanical point of view, as those crystals are key for the load-bearing properties of silk. The simulations also indicated that strands from the crystalline domain interacted with the HAP (001) surface only after losing their initial  $\beta$ -sheet conformation. This agreed with previous experimental data reporting the inability of  $\beta$ -sheet structures to nucleate the biomineralization of HAP.<sup>28</sup>

The amorphous domain was very stable throughout the simulation, as shown by its radius of gyration (*ca.* 21.8 Å throughout the entire simulation). This domain only underwent a partial rearrangement of its secondary structure, with a reduction in random coil regions (from  $58.0 \pm 1.6\%$  in the starting structure to  $51.0 \pm 1.0\%$  during the last 5 ns of simulation) and a rise in turn structures. This was in line with its concomitant rise in intraprotein hydrogen bonds ( $35 \pm 3$  to 45

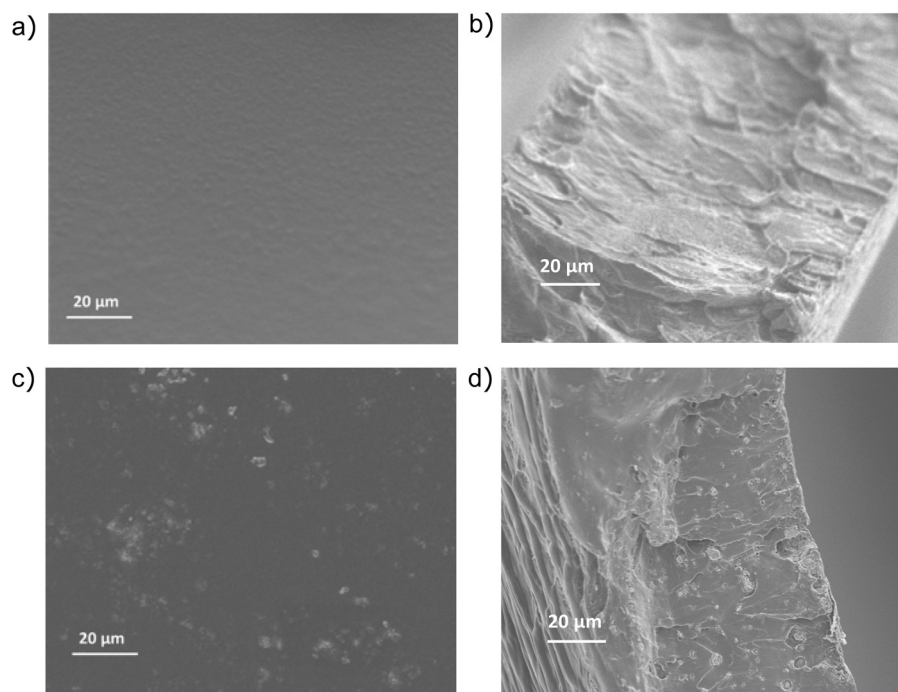


**Fig. 5** Mesostructure characterization: SEM images of the (a) surface and (b) cross-section area of silk films, and the (c) surface and (d) cross-section area of silk-HAP 10 wt% films.





$\pm 2$ ) and the reduction in SASA of the hydrophobic residues ( $55.0 \pm 1.5$  to  $49.6 \pm 0.8$  nm<sup>2</sup>) (Fig. 3e). Close contacts between the amorphous domain and HAP took place mostly through glutamic acids. This agreed with previous experimental data suggesting that the deposition of HAP crystals on silk was templated by the high solvent exposure and the presence of carboxylic acid residues in the amorphous domain.<sup>28,63</sup> The N-terminus was the least affected by the interaction with the HAP (001) surface, highlighting the stability of the cross- $\beta$  structure of its homodimeric structure (Fig. 3r). This domain showed minimal variations in its radius of gyration ( $19.5 \pm 0.1$  to  $19.2 \pm 0.1$  Å), the lowest RMSD of the three domains investigated ( $4.6 \pm 0.1$  Å), and almost negligible variation in SASA, both for hydrophilic (*ca.* 33 nm<sup>2</sup>) and hydrophobic (*ca.* 94 nm<sup>2</sup>) amino acids. The N-terminus is believed to play a key role in the oligomerization of silk into nanofibers,<sup>20</sup> and therefore its high stability might indicate that silk retains its ability to form fibrillar structures in the presence of HAP (001) surfaces.

Overall, these MD simulations suggested that silk interacts with the HAP (001) surface preferentially through disordered regions and *via* charged amino acids. This has implications for the biofabrication of silk-like polypeptides. When designing recombinant silk-like polypeptides, focus is usually placed on utilizing motifs like GAGAGS<sup>64–66</sup> due to their ability to form  $\beta$ -sheet crystals. This usually aims at enhancing the mechanical properties of materials derived from such polypeptides. However, our data highlight the important role of less ordered and/or more charged blocks in enhancing the interfacial interaction between silk and HAP.

FTIR data agreed with MD data, confirming that HAP reduced the  $\beta$ -sheets in silk (Fig. 4b). Given that a high content of  $\beta$ -sheets is connected to a larger strength in silk biomaterials,<sup>67</sup> our results showed the need for postprocessing methods to enhance the mechanical properties of silk–HAP films. To that end, water vapor annealing is a post-synthesis method commonly used to enhance the formation of  $\beta$ -sheets in silk biomaterials to enhance their mechanical properties.<sup>62,68,69</sup> Here, water vapor annealing increased the content of  $\beta$ -sheet structures in films, although this was more effective in the absence of HAP, as shown by FTIR data (Fig. 4c). Even though a reduction in  $\beta$ -sheet crystals would generally be regarded as disadvantageous for the mechanical properties of silk, we hypothesize that it could have two positive effects. First, less  $\beta$ -sheets could enhance the interfacial interaction between HAP and silk, since HAP crystals have shown a preferential nucleation on unstructured regions of silk.<sup>28</sup> In fact, the present work showed that the crystalline domain was only able to interact with the HAP surface only after the  $\beta$ -sheet crystal was disrupted (Fig. 2). And second, silk biomaterials with a high content of  $\beta$ -sheets could limit the adhesion and spreading of cells, possibly due to the lack of contact sites for cellular attachment in  $\beta$ -sheets or the preference of cells to avoid the sharp edges of  $\beta$ -sheet crystals. To that end, recent work showed that the attachment of hMSCs cells and their alkaline phosphatase activity was 2.5 times

larger in silk biomaterials with 25%  $\beta$ -sheets, compared to similar materials with 41%  $\beta$ -sheets.<sup>70</sup> This suggested that lower crystallinity of the surface favored not only cell attachment but also viability and proliferation.<sup>67</sup>

## 5. Conclusion

This combined computational–experimental work described with atomistic resolution the interfacial interaction of the amorphous, crystalline and N-terminus domains of silk in contact with HAP (001) surfaces at pH 7 and the potential implications for the development of osteoinductive silk biomaterials. Overall, this work provided computational data with atomistic resolution to quantify dynamic and structural processes that occur during the formation of silk–HAP composites. HAP (001) surfaces weakened a key mechanical signature of silk (its  $\beta$ -sheet crystals). Conversely, the amorphous and N-terminus domains remained relatively unaltered during the MD simulations. The reduction in  $\beta$ -sheets was also confirmed experimentally by FTIR of silk–HAP films, and could be only partially overcome by water vapor annealing. Even though a reduction in  $\beta$ -sheet crystals would lower the mechanical strength of the silk component, it could facilitate the interaction between silk and HAP, as well as increase cell attachment.

## Author contributions

DLK and MJB acquired funding, conceptualized and supervised this research. DLB, ZMM, AFB and VF conducted the research, analyzed the data, and created the visuals. DLB and AFB developed the computational work and the scripts for analysis. ZMM and VF performed the experimental work. The manuscript was written by all the authors and they have given approval to its final version.

## Data availability

The authors declare that all the relevant data supporting the findings of this study are available within the paper or from the corresponding author upon reasonable request.

## Conflicts of interest

The authors declare that they have no known competing financial interests or personal relationships that could influence the work reported in this.

## Acknowledgements

DLB, ZMM, VF, DLK and MJB acknowledge the support from the National Institutes of Health (U01 EB014976). MJB



acknowledges the support from ONR (N000141612333 and N000141912375) and DLK from the AFOSR (FA9550-17-1-0333). All the authors acknowledge the support from MIT-Spain INDITEX Sustainability Seed Fund project “Multiscale modeling and production of silk-ceramic bone regeneration biomaterials”.

## References

- 1 N. Reznikov, M. Bilton, L. Lari, M. Stevens and R. Kröger, *Science*, 2018, **360**, eaao2189.
- 2 S. Von Euw, Y. Wang, G. Laurent, C. Drouet, F. Babonneau, N. Nassif and T. Azaïs, *Sci. Rep.*, 2019, **9**, 1–11.
- 3 H. Qu, H. Fu, Z. Han and Y. Sun, *RSC Adv.*, 2019, **9**, 26252–26262.
- 4 M. Milazzo, N. Contessi Negrini, S. Scialla, B. Marelli, S. Farè, S. Danti and M. J. Buehler, *Adv. Funct. Mater.*, 2019, **29**, 1903055.
- 5 M. C. Catoira, L. Fusaro, D. Di Francesco, M. Ramella and F. Boccafroschi, *J. Mater. Sci. Mater. Med.*, 2019, **30**, 115.
- 6 O. O. Ige, L. E. Umoru and S. Aribio, *ISRN Mater. Sci.*, 2012, **2012**, 1–20.
- 7 S. Bhatia and S. Bhatia, in *Natural Polymer Drug Delivery Systems*, Springer International Publishing, 2016, pp. 95–118.
- 8 Y. J. Yang, A. L. Holmberg and B. D. Olsen, *Annu. Rev. Chem. Biomol. Eng.*, 2017, **8**, 549–575.
- 9 S. Keten, Z. Xu, B. Ihle and M. J. Buehler, *Nat. Mater.*, 2010, **9**, 359.
- 10 D. Ebrahimi, O. Tokareva, N. G. Rim, J. Y. Wong, D. L. Kaplan and M. J. Buehler, *ACS Biomater. Sci. Eng.*, 2015, **1**, 864–876.
- 11 Y. Wang, J. Guo, L. Zhou, C. Ye, F. G. Omenetto, D. L. Kaplan and S. Ling, *Adv. Funct. Mater.*, 2018, **28**, 1–24.
- 12 X. Wang, Z. Ding, C. Wang, X. Chen, H. Xu, Q. Lu and D. L. Kaplan, *J. Mater. Chem. B*, 2018, **6**, 2739–2746.
- 13 D. López Barreiro, Z. Martín-Moldes, J. Yeo, S. Shen, M. J. Hawker, F. J. Martín-Martínez, D. L. Kaplan and M. J. Buehler, *Adv. Mater.*, 2019, **31**, 1904720.
- 14 S. Ling, K. Jin, D. L. Kaplan and M. J. Buehler, *Nano Lett.*, 2016, **16**, 3795–3800.
- 15 C. Fu, Z. Shao and V. Fritz, *Chem. Commun.*, 2009, 6515–6529.
- 16 S.-W. Ha, H. S. Gracz, A. E. Tonelli and S. M. Hudson, *Biomacromolecules*, 2005, **6**, 2563–2569.
- 17 C.-Z. Zhou, F. Confalonieri, M. Jacquet, R. Perasso, Z.-G. Li and J. Janin, *Proteins: Struct., Funct., Bioinf.*, 2001, **44**, 119–122.
- 18 G. Chen, N. Matsuhisa, Z. Liu, D. Qi, P. Cai, Y. Jiang, C. Wan, Y. Cui, W. R. Leow, Z. Liu, S. Gong, K. Zhang, Y. Cheng and X. Chen, *Adv. Mater.*, 2018, **30**, 1800129.
- 19 W. Huang, S. Ling, C. Li, F. G. Omenetto and D. L. Kaplan, *Chem. Soc. Rev.*, 2018, **47**, 6486–6504.
- 20 D. P. Tran, V. T. Lam, T. L. Tran, T. N. S. Nguyen and H. T. Thi Tran, *Phys. Chem. Chem. Phys.*, 2018, **20**, 19240–19249.
- 21 Z. Ding, Z. Fan, X. Huang, Q. Lu, W. Xu and D. L. Kaplan, *ACS Appl. Mater. Interfaces*, 2016, **8**, 24463–24470.
- 22 H. H. K. Xu, P. Wang, L. Wang, C. Bao, Q. Chen, M. D. Weir, L. C. Chow, L. Zhao, X. Zhou and M. A. Reynolds, *Bone Res.*, 2017, **5**, 17056.
- 23 M. Farokhi, F. Mottaghiab, S. Samani, M. A. Shokrgozar, S. C. Kundu, R. L. Reis, Y. Fatahi and D. L. Kaplan, *Biotechnol. Adv.*, 2018, **36**, 68–91.
- 24 A. J. Mieszkawska, N. Fourligas, I. Georgakoudi, N. M. Ouhib, D. J. Belton, C. C. Perry and D. L. Kaplan, *Biomaterials*, 2010, **31**, 8902–8910.
- 25 Z. Martín-Moldes, D. Ebrahimi, R. Plowright, N. Dinjaski, C. C. Perry, M. J. Buehler and D. L. Kaplan, *Adv. Funct. Mater.*, 2017, **28**, 1702570.
- 26 Q. Fu, E. Saiz, M. N. Rahaman and A. P. Tomsia, *Mater. Sci. Eng., C*, 2011, **31**, 1245–1256.
- 27 X. Du, D. Wei, L. Huang, M. Zhu, Y. Zhang and Y. Zhu, *Mater. Sci. Eng., C*, 2019, **103**, 109731.
- 28 B. Marelli, C. E. Ghezzi, A. Alessandrino, J. E. Barralet, G. Freddi and S. N. Nazhat, *Biomaterials*, 2012, **33**, 102–108.
- 29 S. Ling, Z. Qin, W. Huang, S. Cao, D. L. Kaplan and M. J. Buehler, *Sci. Adv.*, 2017, **3**, e1601939.
- 30 S. Bhumiratana, W. L. Grayson, A. Castaneda, D. N. Rockwood, E. S. Gil, D. L. Kaplan and G. Vunjak-Novakovic, *Biomaterials*, 2011, **32**, 2812–2820.
- 31 F. A. Sheikh, H. W. Ju, B. M. Moon, H. J. Park, J. H. Kim, O. J. Lee and C. H. Park, *Nanoscale Res. Lett.*, 2013, **8**, 303.
- 32 X. Huang, S. Bai, Q. Lu, X. Liu, S. Liu and H. Zhu, *J. Biomed. Mater. Res., Part B*, 2015, **103**, 1402–1414.
- 33 Z. Ding, H. Han, Z. Fan, H. Lu, Y. Sang, Y. Yao, Q. Cheng, Q. Lu and D. L. Kaplan, *ACS Appl. Mater. Interfaces*, 2017, **9**, 16913–16921.
- 34 V. Fitzpatrick, Z. Martín-Moldes, A. Deck, R. Torres-Sanchez, A. Valat, D. Cairns, C. Li and D. L. Kaplan, *Biomaterials*, 2021, **276**, 120995.
- 35 Y. Jin, B. Kundu, Y. Cai, S. C. Kundu and J. Yao, *Colloids Surf., B*, 2015, **134**, 339–345.
- 36 H. Liu, G. W. Xu, Y. F. Wang, H. S. Zhao, S. Xiong, Y. Wu, B. C. Heng, C. R. An, G. H. Zhu and D. H. Xie, *Biomaterials*, 2015, **49**, 103–112.
- 37 N. Dinjaski, R. Plowright, S. Zhou, D. J. Belton, C. C. Perry and D. L. Kaplan, *Acta Biomater.*, 2017, **49**, 127–139.
- 38 F. Barthelat, Z. Yin and M. J. Buehler, *Nat. Rev. Mater.*, 2016, **1**, 16007.
- 39 Y. Cheng, L.-D. Koh, D. Li, B. Ji, Y. Zhang, J. Yeo, G. Guan, M.-Y. Han and Y.-W. Zhang, *ACS Appl. Mater. Interfaces*, 2015, **7**, 21787–21796.
- 40 A. M. Grant, H. S. Kim, T. L. Dupnock, K. Hu, Y. G. Yingling and V. V. Tsukruk, *Adv. Funct. Mater.*, 2016, **26**, 6380–6392.
- 41 S. Ling, K. Jin, Z. Qin, C. Li, K. Zheng, Y. Zhao, Q. Wang, D. L. Kaplan and M. J. Buehler, *Adv. Mater.*, 2018, **30**, 1802306.
- 42 S. J. Segvich, H. C. Smith and D. H. Kohn, *Biomaterials*, 2009, **30**, 1287–1298.



- 43 S. Segvich, S. Biswas, U. Becker and D. H. Kohn, *Cells Tissues Organs*, 2009, **189**, 245–251.
- 44 T.-J. Lin and H. Heinz, *J. Phys. Chem. C*, 2016, **120**, 4975–4992.
- 45 A. Rimola, M. Corno, J. Garza and P. Ugliengo, *Philos. Trans. R. Soc., A*, 2012, **370**, 1478–1498.
- 46 X. Dong, Q. Wang, T. Wu and H. Pan, *Biophys. J.*, 2007, **93**, 750–759.
- 47 J.-W. Shen, T. Wu, Q. Wang and H.-H. Pan, *Biomaterials*, 2008, **29**, 513–532.
- 48 H. Heinz, T.-J. Lin, R. K. Mishra and F. S. Emami, *Langmuir*, 2013, **29**, 1754–1765.
- 49 Materials Studio, <https://www.3ds.com/products-services/biovia/products/molecular-modeling-simulation/biovia-materials-studio/>, (accessed 31 January 2021).
- 50 Y.-X. He, N.-N. Zhang, W.-F. Li, N. Jia, B.-Y. Chen, K. Zhou, J. Zhang, Y. Chen and C.-Z. Zhou, *J. Mol. Biol.*, 2012, **418**, 197–207.
- 51 J. C. Phillips, R. Braun, W. Wang, J. Gumbart, E. Tajkhorshid, E. Villa, C. Chipot, R. D. Skeel, L. Kalé and K. Schulten, *J. Comput. Chem.*, 2005, **26**, 1781–1802.
- 52 B. R. Brooks, C. L. Brooks III, A. D. Mackerell, Jr., L. Nilsson, R. J. Petrella, B. Roux, Y. Won, G. Archontis, C. Bartels, S. Boresch, A. Caflisch, L. Caves, Q. Cui, A. R. Dinner, M. Feig, S. Fischer, J. Gao, M. Hodoscek, W. Im, K. Kuczera, T. Lazaridis, J. Ma, V. Ovchinnikov, E. Paci, R. W. Pastor, C. B. Post, J. Z. Pu, M. Schaefer, B. Tidor, R. M. Venable, H. L. Woodcock, X. Wu, W. Yang, D. M. York and M. Karplus, *J. Comput. Chem.*, 2009, **30**, 1545–1614.
- 53 J.-P. Ryckaert, G. Ciccotti and H. J. C. Berendsen, *J. Comput. Phys.*, 1977, **23**, 327–341.
- 54 W. Humphrey, A. Dalke and K. Schulten, *J. Mol. Graphics*, 1996, **14**, 33–38.
- 55 D. Frishman and P. Argos, *Proteins: Struct., Funct., Bioinf.*, 1995, **23**, 566–579.
- 56 D. N. Rockwood, R. C. Preda, T. Yücel, X. Wang, M. L. Lovett and D. L. Kaplan, *Nat. Protoc.*, 2011, **6**, 1612.
- 57 S. Zhou, W. Huang, D. J. Belton, L. O. Simmons, C. C. Perry, X. Wang and D. L. Kaplan, *Acta Biomater.*, 2015, **15**, 173–180.
- 58 J. Bandekar, *Biochim. Biophys. Acta, Protein Struct. Mol. Enzymol.*, 1992, **1120**, 123–143.
- 59 H. Yang, S. Yang, J. Kong, A. Dong and S. Yu, *Nat. Protoc.*, 2015, **10**, 382–396.
- 60 S. Ling, N. Dinjaski, D. Ebrahimi, J. Y. Wong, D. L. Kaplan and M. J. Buehler, *ACS Biomater. Sci. Eng.*, 2016, **2**, 1298–1308.
- 61 J. Ming, Z. Liu, S. Bie, F. Zhang and B. Zuo, *Mater. Sci. Eng., C*, 2014, **37**, 48–53.
- 62 X. Hu, D. Kaplan and P. Cebe, *Macromolecules*, 2006, **39**, 6161–6170.
- 63 A. Takeuchi, C. Ohtsuki, T. Miyazaki, M. Kamitakahara, S. Ogata, M. Yamazaki, Y. Furutani, H. Kinoshita and M. Tanihara, *J. R. Soc., Interface*, 2005, **2**, 373–378.
- 64 Q. Wang, X. Xia, W. Huang, Y. Lin, Q. Xu and D. L. Kaplan, *Adv. Funct. Mater.*, 2014, **24**, 4303–4310.
- 65 A. Ibáñez-Fonseca, D. Orbanic, F. J. Arias, M. Alonso, D. I. Zeugolis and J. C. Rodríguez-Cabello, *Small*, 2020, **16**, 2001244.
- 66 M. D. Golinska, M. K. Włodarczyk-Biegun, M. W. T. Werten, M. A. C. Stuart, F. A. de Wolf and R. de Vries, *Biomacromolecules*, 2014, **15**, 699–706.
- 67 X. Hu, K. Shmelev, L. Sun, E. S. Gil, S. H. Park, P. Cebe and D. L. Kaplan, *Biomacromolecules*, 2011, **12**, 1686–1696.
- 68 Q. Lu, X. Hu, X. Wang, J. A. Kluge, S. Lu, P. Cebe and D. L. Kaplan, *Acta Biomater.*, 2010, **6**, 1380–1387.
- 69 C. Malinowski, F. He, Y. Zhao, I. Chang, D. W. Hatchett, S. Zhai and H. Zhao, *RSC Adv.*, 2019, **9**, 40792–40799.
- 70 Z. Wenhao, T. Zhang, J. Yan, Q. Li, P. Xiong, Y. Li, Y. Cheng and Y. Zheng, *Acta Biomater.*, 2020, **116**, 223–245.

